Fast reconstruction of atomic-scale STEM-EELS images from sparse sampling – Supplementary materials

Etienne Monier[(1)], Thomas Oberlin[(1)], Nathalie Brun[(2)],
Xiaoyan Li[(2)], Marcel Tencé[(2)], Nicolas Dobigeon[(1)]
[(1)] University of Toulouse, IRIT/INP-ENSEEIHT, 31071 Toulouse Cedex 7, France
email: {etienne.monier, thomas.oberlin, nicolas.dobigeon}@enseeiht.fr
[(2)] Laboratoire de Physique des Solides, CNRS, Univ. Paris-Sud, Univ. Paris-Saclay, 91405 Orsay Cedex, France
email: {nathalie.brun, xiaoyan.li, marcel.tence}@u-psud.fr

TECHNICAL REPORT – 2020, February
University of Toulouse, IRIT/INP-ENSEEIHT
2 rue Camichel, BP 7122, 31071 Toulouse cedex 7, France

This report provides complementary results in support of the paper [1].

I. CLS PERFORMANCE WITHOUT PCA

In [1, Section 3.2], PCA is a considered as preprocessing step of the proposed CLS algorithm. Indeed, performing PCA as a preprocessing step has the following advantages. First, it implicitly introduces a spectral regularization of the inverse problem by imposing a low-rank structure of the solution. Similar strategies have been widely promoted for various tasks conducted on multiband images, including compressive senssing [2], [3], inpainting [4], [5], fusion [6]–[8] or mixture analysis [9], [10]. Second, by reducing the amount of data to process, it allows the computational time to be significantly reduced. This preprocessing may induce some reconstruction artefacts when the estimation of the covariance matrix is not accurate, e.g., in case of a low sampling ratio. Moreover, some low-powerful structures may disappear when keeping a too small number of principal components [11].

Part of this work has been funded by CNRS, France, through the Imag'in ARSIS project, the METSA 17A304 program and the ANR-3IA Artificial and Natural Intelligence Toulouse Institute (ANITI) under grant agreement ANR-19-PI3A-0004. This project has received funding from the European Union's Horizon 2020 Research and Innovation Programme under grant agreement no 823717.

We propose to illustrate the reconstruction performance improvement brought by PCA as a pre-processing. To that end, for several sampling ratio, we propose to reconstruct the semi-real image $\mathbf{R}_2^*$ with CLS when it is preceded or not by PCA. The reconstruction performance, in terms of SNR, aSAD and SSIM, and the execution times are given as functions of the sampling ratio in Figures 1a, 1b, 1c and 1d respectively. For all metrics and sampling ratios, performing PCA as a preprocessing improves the reconstruction performance. Moreover, it allows the execution times to be reduced by a factor of 200. Last, Figure 2 shows the reconstructed images around three main edges when PCA is applied and when it is not (for a sampling ratio of 20%). No particular visual difference can be observed between the two procedures.

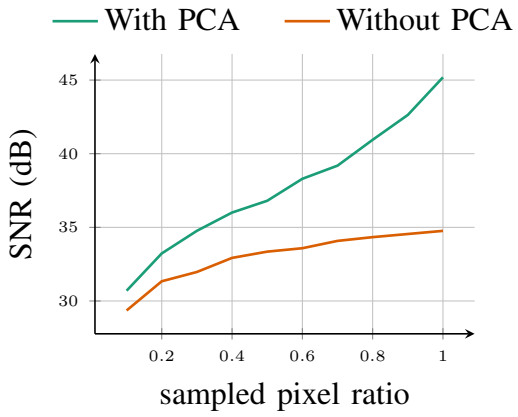

(a) Evolution of SNR w.r.t. sampling ratio.

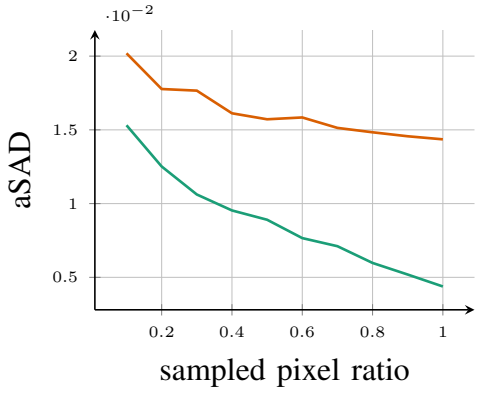

(b) Evolution of aSAD w.r.t. sampling ratio.

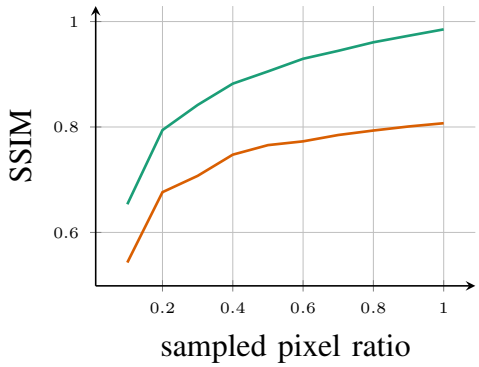

(c) Evolution of SSIM w.r.t. sampling ratio.

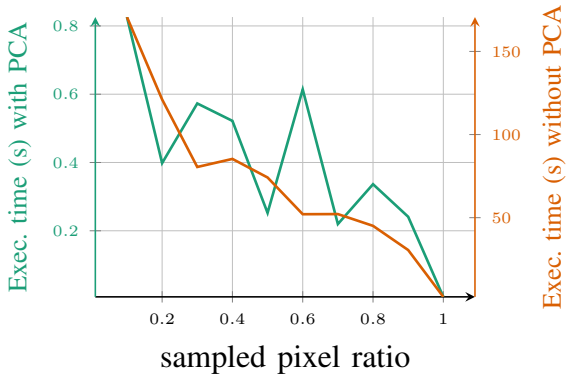

(d) Evolution of execution time w.r.t. sampling ratio.

Fig. 1: Performance of reconstruction and execution times as functions of the sampling ratio for the semi-real image $\mathbf{R}_2^*$ with CLS when it is preceded or not by PCA.

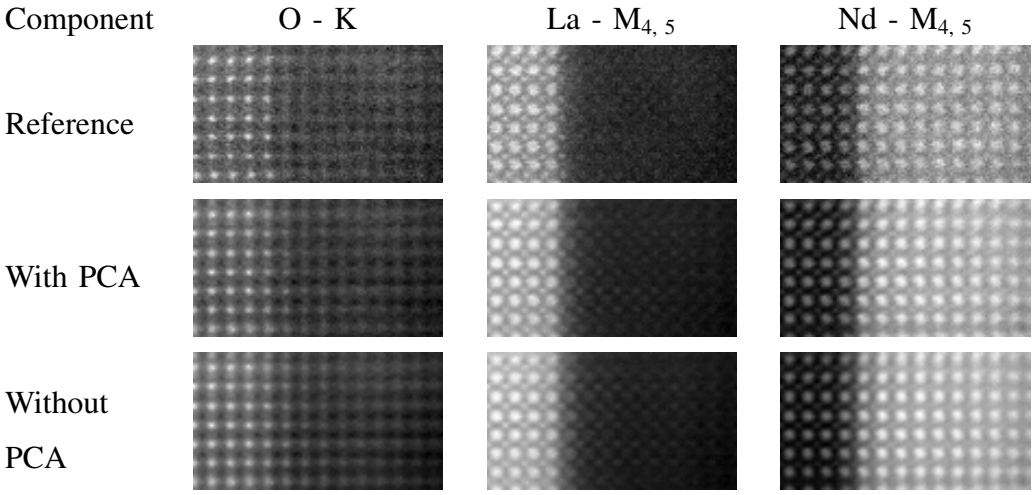

Fig. 2: Reconstruction results for $\mathbf{R}_2^*$ with PCA (middle) or without PCA (bottom) as a preprocessing step. The images show the sum of 5 bands around 3 particular edges ($\mathrm{O}-\mathrm{K}$, $\mathrm{La}-\mathrm{M}_{4,5}$ and $\mathrm{Nd}-\mathrm{M}_{4,5}$). The reference corresponds to the semi-real image $\mathbf{R}_2^*$.

II. CLS PARAMETER ESTIMATION BASED ON THE NOISE LEVEL ESTIMATION

Inspired by the strategy in [4], the regularization parameter λ of the CLS algorithm can be adjusted following the dichotomy approach, as discussed in [1, Section 3.2]. More precisely, the experimenter usually has some knowledge about the image to be reconstructed such as the noise level (which can be estimated beforehand) or the sparsity level, i.e., the ratio of non-zero coefficients of the DCT representation. This prior knowledge can be used to assess the quality of the solution $\hat{\mathbf{X}}_\lambda$ obtained by CLS for a given value λ of the regularization parameter. Indeed, the fidelity term $\frac{1}{2}\|\mathbf{Y}-\hat{\mathbf{X}}_\lambda\mathbf{\Phi}\|_{\mathrm{F}}^2$ should be of the order of magnitude of the noise level. Moreover, this residual term (resp. the sparsity-promoting term $\|\hat{\mathbf{X}}_\lambda\mathbf{\Psi}\|_{2,1}$) is expected to increase (resp. to decrease) with the CLS parameter λ. Thus a dichotomic search can be conducted to adjust the regularization parameter automatically. It consists in running the CLS algorithm, computing the fidelity term obtained at convergence, and running a new instance of CLS after increasing or decreasing the regularization parameter until reaching a value of the fidelity term close to the noise level. For instance, a similar strategy has been successfully followed in [4].

To illustrate this, under the experimental protocol described in the paper, CLS is applied to reconstruct the $\mathbf{R}_2^*$ image for a wide range of parameter values λ. The reconstruction performance, in term of SNR, is depicted in Figure 3 as a function of λ. In this figure, the parameter adjusted

thanks to the dichotomy search is spotted as a orange dot while the optimal parameter (i.e., leading to the best reconstruction) appears in red. This result shows that the proposed strategy to automatically adjust the regularization parameter provides reconstruction performance close to the optimal one.

Note however that, for all methods compared in the experiments reported in [1, Section 5], the performance results are those obtained for an optimal choice of the algorithmic parameters, i.e., reaching the best performance given by the methods.

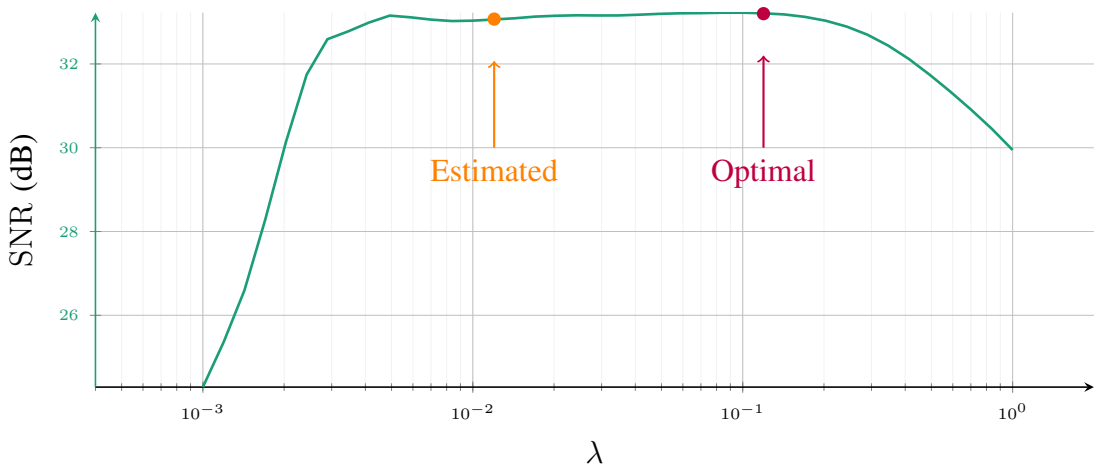

Fig. 3: CLS parameter estimation process. $\mathbf{R}_2^*$ is reconstructed using CLS for a range of parameter values and the SNR performance is computed for each value of λ. The parameter adjusted thanks to the dichotomy search is spotted as a orange dot while the optimal parameter (i.e., leading to the best reconstruction) appears in red. This result shows that the proposed strategy to automatically adjust the regularization parameter provides reconstruction performance close to the optimal one.

III. Reconstruction in case of mixed Poisson-Gaussian noise

In the experiments reported in [1, Section 5], the semi-real images are corrupted by an additive Gaussian white noise. Yet, this assumption can be questionable as microscopy data is expected to be corrupted by a mixed Poisson-Gaussian noise. Since the proportions of the two noise components in this mixture are difficult to infer, we decided to consider a Gaussian noise only in our experiments.

To highlight the robustness of CLS in case of mixed Poisson-Gaussian noise, the $\bar{\mathbf{R}}_2$ noise-free image has been degraded using the two following procedures:

- $\mathcal{P}_{\mathrm{G}}$: additive Gaussian noise with variance σ^2 was added to $\bar{\mathbf{R}}_2$ to yield the corrupted image denoted $\mathbf{R}_2^{(\mathrm{G})}$,
- $\mathcal{P}_{\mathrm{PG}}$: Poisson noise with variance $\sigma^2/2$ was applied to $\bar{\mathbf{R}}_2$ followed by additive Gaussian noise with variance $\sigma^2/2$ to yield the corrupted image denoted $\mathbf{R}_2^{(\mathrm{PG})}$.

Note that the two generated noisy images $\mathbf{R}_2^{(\mathrm{G})}$ and $\mathbf{R}_2^{(\mathrm{PG})}$ exhibit the same overall level of noise σ^2. They are subsampled with a ratio of 20%, and then reconstructed using NN, 3S and CLS. The reconstruction performances in term of SNR are reported in Table I for two noise levels σ^2. These results show that the method performances do not significantly degrade when considering a more realistic mixed noise.

	σ^2		$10^4 \times \sigma^2$	
	$\mathcal{P}_{\mathrm{G}}$	$\mathcal{P}_{\mathrm{PG}}$	$\mathcal{P}_{\mathrm{G}}$	$\mathcal{P}_{\mathrm{PG}}$
NN	28.71	28.71	25.17	24.85
3S	30.17	30.18	28.02	28.05
CLS	33.15	33.15	29.05	28.67

TABLE I: Reconstruction performance (as SNR in dB) for images $\mathbf{R}_2^{(\mathrm{G})}$ and $\mathbf{R}_2^{(\mathrm{PG})}$. The results are similar for both corruption processes $\mathcal{P}_{\mathrm{G}}$ and $\mathcal{P}_{\mathrm{PG}}$, which shows that CLS is not particularly impacted by Poisson noise.

IV. Synthetic results error maps

In [1, Section 5], we study the reconstruction performance thanks to experiments conducted on synthetic and semi-real images. The results show the interest of CLS as a fast and efficient trade-off. This is confirmed in [1, Section 5.3] for real images with the Figure 5 which shows three main signatures bands for all methods. We propose here to produce a similar figure for synthetic images. To that end, the corresponding error in term of NMSE is represented in Figure 4. This representation can be useful to locate the main reconstruction errors. Moreover, Figure 5 shows the error histograms for each edge. They show that the NN error is globally larger than the other methods and particularly high for some pixels.

V. Performance comparison for several sampling ratios

The proposed CLS method is able to work for any sampling ratio. However, in case of PCA pre-processing, reducing the sampling ratio may degrade the quality of the covariance matrix

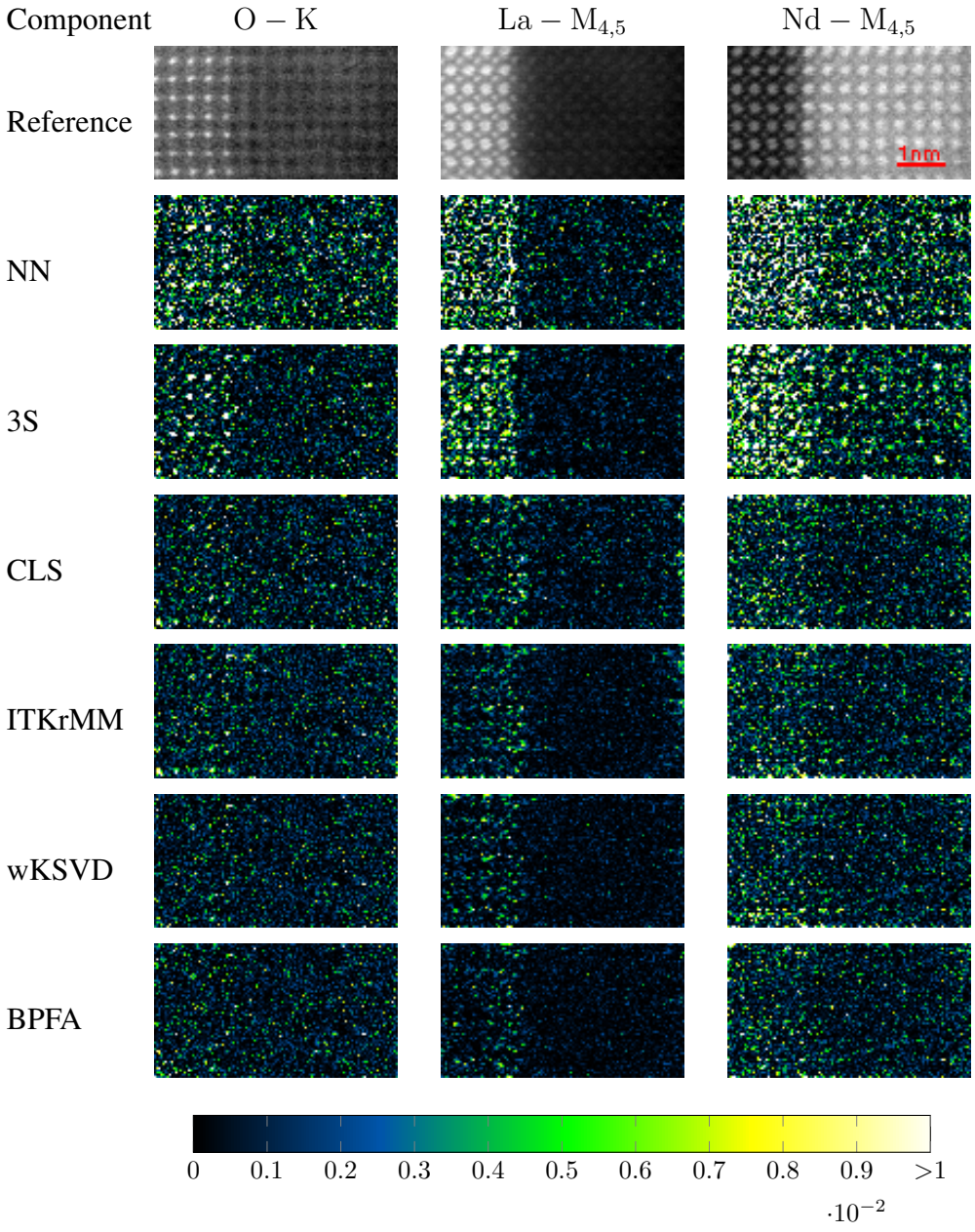

Fig. 4: Reconstruction error for $\mathbf{R}_2^*$ in term of NMSE around 3 particular edges ($\mathrm{O}-\mathrm{K}$, $\mathrm{La}-\mathrm{M}_{4,5}$ and $\mathrm{Nd}-\mathrm{M}_{4,5}$). The dynamic is the same for all images, i.e., they can be compared through the methods and signatures. The reference corresponds to the noise-free image $\bar{\mathbf{R}}_2$.

estimation. In particular, when the number of acquired pixels is smaller than the number of bands (i.e., in a so called "large p, small n" setting), shrinkage estimation of the covariance matrix may be needed to cope with the unstability of the conventional maximum likelihood estimators [12]. In our experiments, the full images are composed of 10.000 pixels while the number of spectral bands is around 1.500. By choosing a pixel ratio of 0.2, we ensure that the number of acquired pixels is at least slightly greater than the number of bands, thus ensuring the well-posedness of the covariance matrix estimation.

As a complementary insight, the performances of the compared algorithms have been evaluated when reconstructing the semi-real image $\mathbf{R}_2^*$ for various sampling ratios. The results are reported in in Table II. As expected, the performances of all methods increase with the sampling ratio. It is worth noting that the proposed algorithm still perform wells for low and high sampling ratios (i.e., 5% and 50%).

VI. Performance in case of vacancies

The presence of vacancies may degrade the reconstruction performance for all methods. CLS is expected to be impacted as its regularization favors periodic reconstructions (see Section 3.2). Conversely, dictionary-learning-based (DL) methods is expected to suffer from vacancy representation deficiency. Indeed, since the vacancy is rare, it is very unlikely to learn atoms able to sparsely represent it.

To illustrate this impact, a new synthetic spectrum-image denoted $\mathbf{S}_{\mathrm{v}}^*$ has been generated similarly to the synthetic image $\mathbf{S}^*$, except that two atoms initially located on both sides of the interface have been switched, which mimics the presence of vacancies.

Table III reports the reconstruction performances obtained on the images $\mathbf{S}^*$ and $\mathbf{S}_{\mathrm{v}}^*$. Figures 6 and Figure 7 shows the error maps (in term of NMSE) associated with the two images $\mathbf{S}^*$ and $\mathbf{S}_{\mathrm{v}}^*$, respectively, computed around three particular edges. We observe that NN and 3S are not impacted by the presence of the vacancy. Meanwhile, the performances of CLS and DL-based methods, in particular ITKrMM, are degraded. This degradation is particularly visible in the error maps associated with the component $\mathrm{La} - \mathrm{M}_{4,5}$. We observe that the errors of NN and 3S methods are globally the same across all atoms while, for CLS and DL-based methods, errors are located around the vacancies.

To conclude, in case of vacancies, the performance of CLS is not significantly degraded when compared to DL-based methods.

Sampl. ratio	0.05	0.1	0.2	0.3	0.5
NN	24.81	26.42	28.71	29.91	32.04
3S	26.89	27.76	30.17	31.77	34.92
CLS	29.31	30.84	33.15	34.56	37.10
ITKrMM	29.75	31.82	33.67	34.14	34.57
wKSVD	25.51	29.63	34.52	35.52	35.90

(a) SNR performance - Noisy image: 26.75dB.

Sampl. ratio	0.05	0.1	0.2	0.3	0.5
NN	2.846	2.325	1.815	1.542	1.148
3S	2.358	2.041	1.496	1.217	0.857
CLS	1.795	1.539	1.233	1.076	0.856
ITKrMM	1.662	1.406	1.253	1.198	1.163
wKSVD	2.740	1.690	1.163	1.086	1.072

(b) aSAD performance ($\times 100$) - Noisy image: 4.613.

Sampl. ratio	0.05	0.1	0.2	0.3	0.5
NN	0.233	0.425	0.635	0.720	0.823
3S	0.216	0.369	0.621	0.742	0.877
CLS	0.545	0.660	0.790	0.843	0.911
ITKrMM	0.620	0.757	0.819	0.831	0.844
wKSVD	0.499	0.717	0.841	0.858	0.866

(c) SSIM performance - Noisy image: 0.460.

TABLE II: Reconstruction performance in terms of SNR, aSAD and SSIM for the semi-real image $\mathbf{R}_2^*$ for various sampling ratios. The metrics were also computed for the noisy image $\mathbf{R}_2^*$ as a reference.

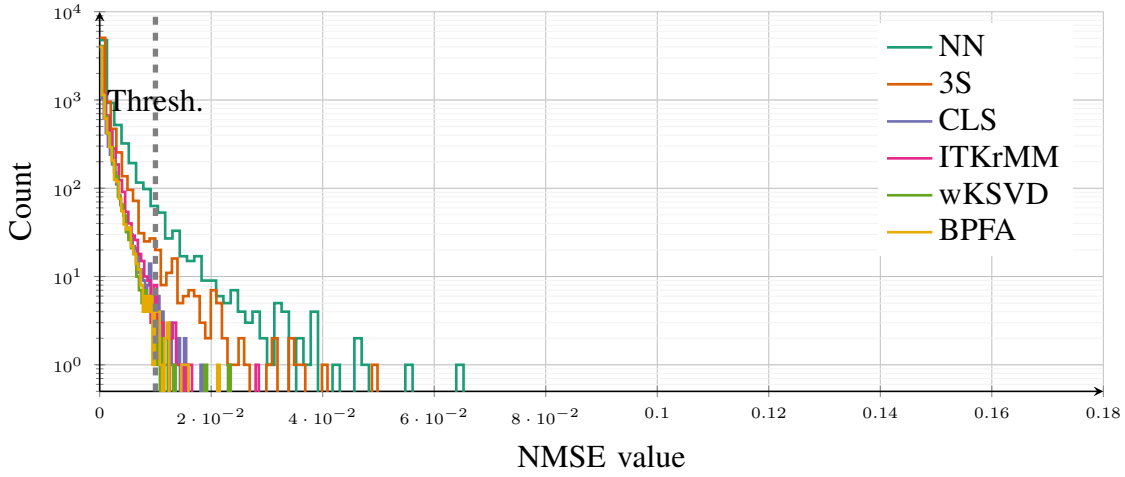

(a) Component $\mathrm{O}-\mathrm{K}$

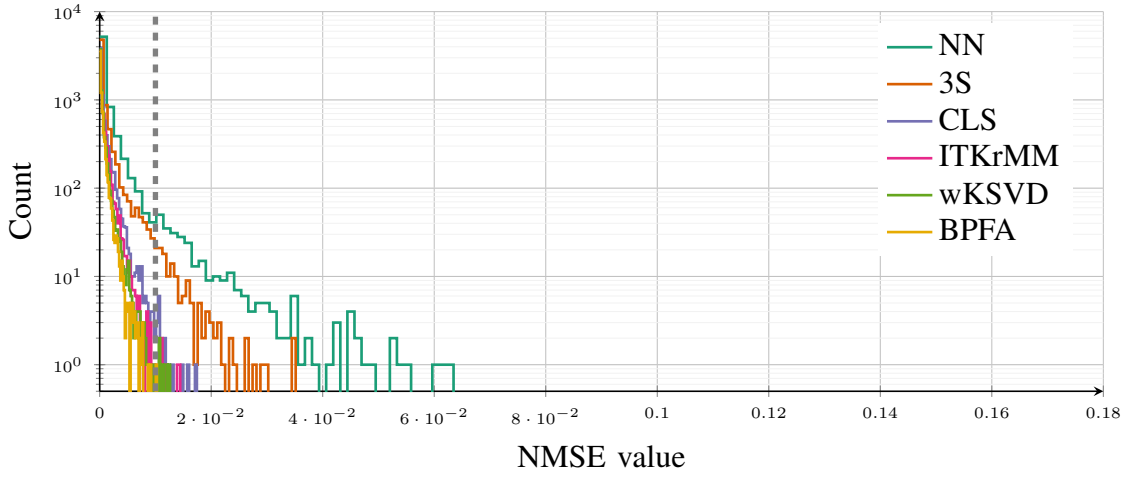

(b) Component $\mathrm{La}-\mathrm{M}_{4,5}$

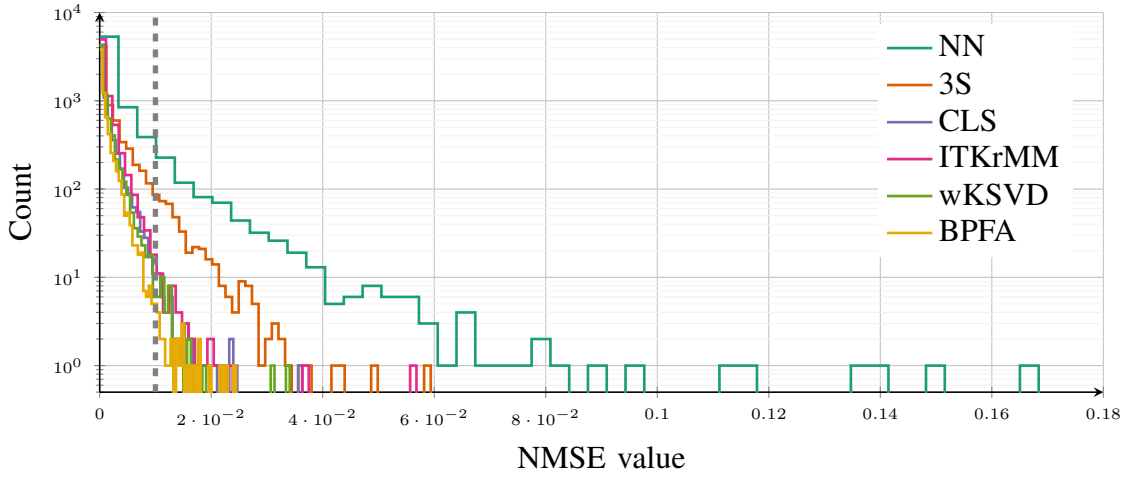

(c) Component $\mathrm{Nd}-\mathrm{M}_{4,5}$

Fig. 5: Histogram of the reconstruction error for $\mathbf{R}_2^*$ in term of NMSE around 3 particular edges ($\mathrm{O}-\mathrm{K}$, $\mathrm{La}-\mathrm{M}_{4,5}$ and $\mathrm{Nd}-\mathrm{M}_{4,5}$). The threshold used to saturate the images in Figure 4 is represented as a dashed gray line. We observe that NN errors are globally larger than for other methods.

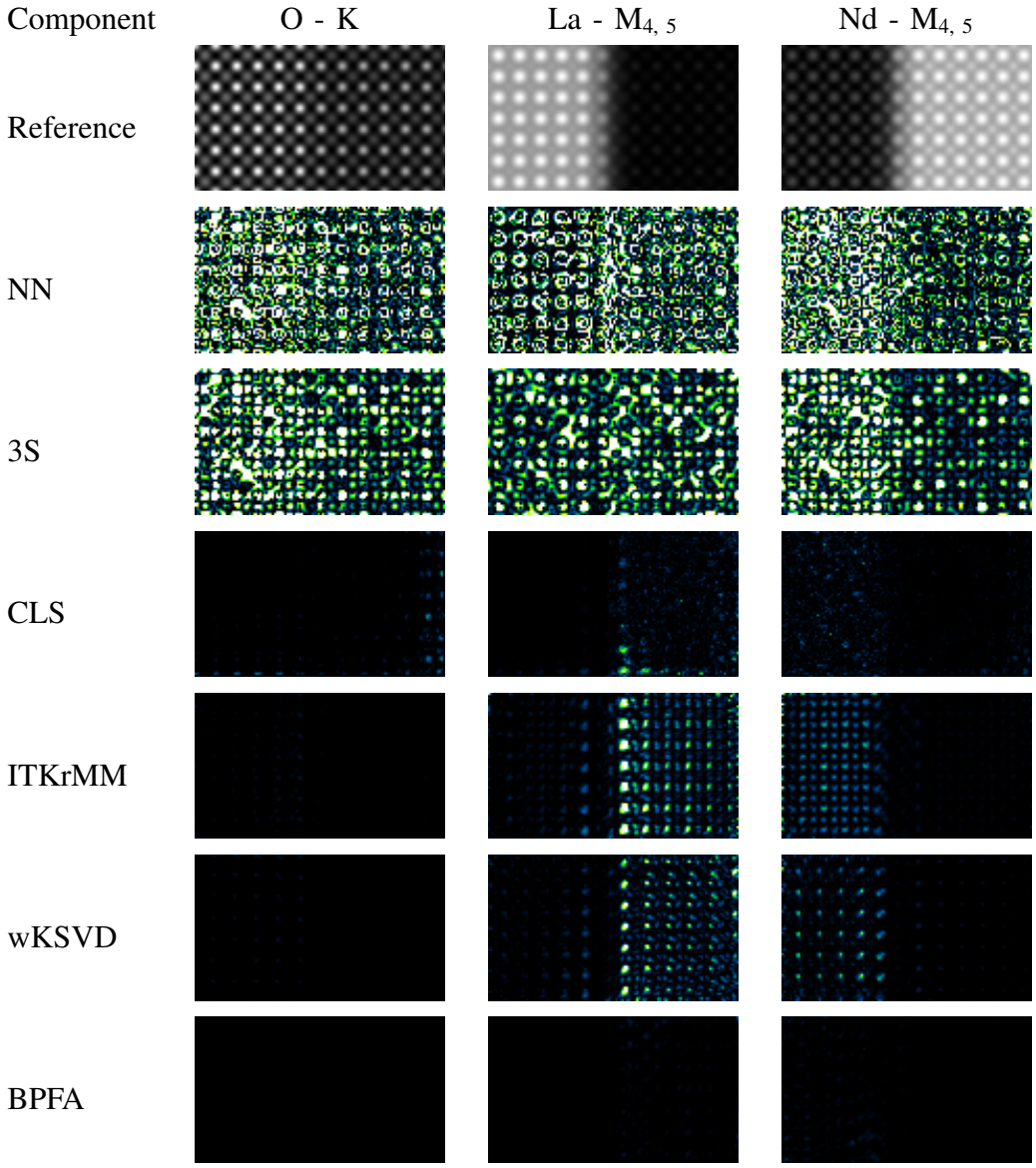

Fig. 6: Reconstruction error for $\mathbf{S}^*$ in term of NMSE around 3 particular edges ($\mathrm{O}-\mathrm{K}$, $\mathrm{La}-\mathrm{M}_{4,5}$ and $\mathrm{Nd}-\mathrm{M}_{4,5}$). The dynamic is the same for all images, i.e., they can be compared through the methods and signatures. The reference synthetic spectrum-image bands are also given for comparison in the first row.

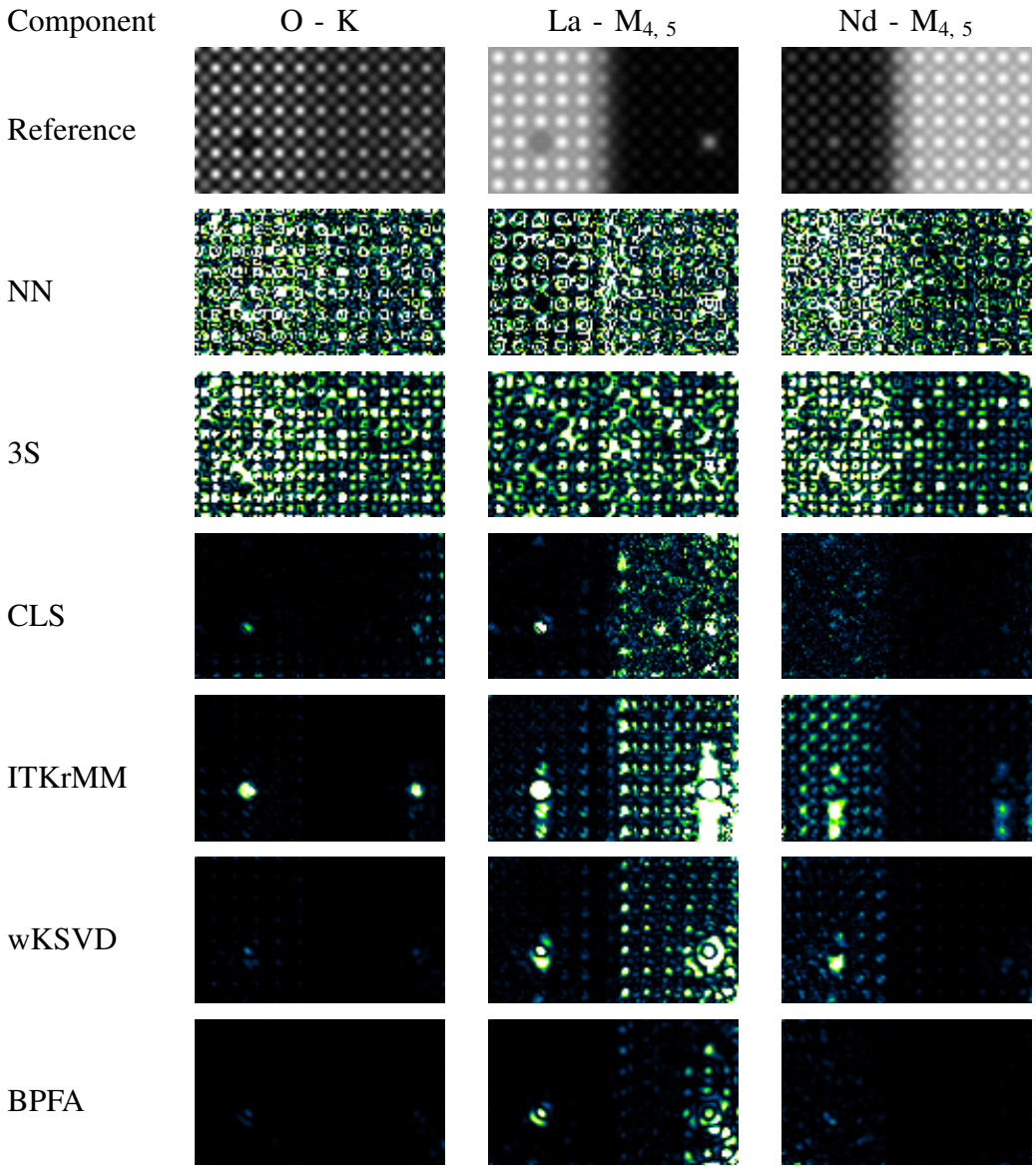

Fig. 7: Reconstruction error for $\mathbf{S}_{\mathrm{v}}^{*}$ in term of NMSE around 3 particular edges ($\mathrm{O}-\mathrm{K}$, $\mathrm{La}-\mathrm{M}_{4,5}$ and $\mathrm{Nd}-\mathrm{M}_{4,5}$). The dynamic is the same for all images, i.e., they can be compared through the methods and signatures. The reference synthetic spectrum-image bands are also given for comparison in the first row. The presence of vacancies degrade the reconstruction performance of CLS and dictionary-based methods.

Method	Without vacancy			With vacancy		
	SNR	aSAD (100×)	SSIM	SNR	aSAD (100×)	SSIM
NN	21.32	1.462	0.735	21.32	1.475	0.738
3S	22.12	1.174	0.710	22.13	1.181	0.715
CLS	42.14	0.224	0.997	38.45	0.346	0.993
ITKrMM	44.16	0.338	0.998	34.34	0.649	0.987
wKSVD	45.59	0.277	0.999	41.49	0.376	0.997
BPFA	52.70	0.150	1.000	45.27	0.236	0.998

TABLE III: Reconstruction performance with and without vacancy.

REFERENCES

[1] E. Monier, T. Oberlin, N. Brun, M. Tencé, M. de Frutos, and N. Dobigeon, "Fast reconstruction of atomic-scale STEM-EELS images from sparse sampling," *Ultramicroscopy*, Feb. 2020, submitted.

[2] Q. Zhang, R. Plemmons, D. Kittle, D. Brady, and S. Prasad, "Joint segmentation and reconstruction of hyperspectral data with compressed measurements," *Appl. Opt.*, vol. 50, no. 22, pp. 4417–4435, 2011.

[3] G. Martín, J. M. Bioucas-Dias, and A. Plaza, "Hyca: A new technique for hyperspectral compressive sensing," *IEEE Trans. Geosci. Remote Sens.*, vol. 53, no. 5, pp. 2819–2831, 2014.

[4] E. Monier, T. Oberlin, N. Brun, M. Tencé, M. de Frutos, and N. Dobigeon, "Reconstruction of partially sampled multiband images – Application to STEM-EELS imaging," *IEEE Trans. Comput. Imag.*, vol. 4, no. 4, pp. 585 – 598, Dec. 2018.

[5] L. Zhuang and J. M. Bioucas-Dias, "Fast hyperspectral image denoising and inpainting based on low-rank and sparse representations," *IEEE J. Sel. Topics Appl. Earth Observations Remote Sens.*, vol. 11, no. 3, pp. 730–742, 2018.

[6] E. Wycoff, T.-H. Chan, K. Jia, W.-K. Ma, , and Y. Ma, "Non-negative sparse promoting algorithm for high resolution hyperspectral imaging," in *Proc. IEEE Int. Conf. Acoust., Speech and Signal Process. (ICASSP)*, Vancouver, Canada, 2013.

[7] M. Simões, J. Bioucas Dias, L. Almeida, and J. Chanussot, "A convex formulation for hyperspectral image superresolution via subspace-based regularization," *IEEE Trans. Geosci. Remote Sens.*, vol. 6, no. 53, pp. 3373–3388, June 2015.

[8] Q. Wei, N. Dobigeon, and J.-Y. Tourneret, "Fast fusion of multi-band images based on solving a Sylvester equation," *IEEE Trans. Image Processing*, vol. 24, no. 11, pp. 4109–4121, Nov. 2015.

[9] N. Dobigeon, S. Moussaoui, M. Coulon, J.-Y. Tourneret, and A. O. Hero, "Joint Bayesian endmember extraction and linear unmixing for hyperspectral imagery," *IEEE Trans. Signal Processing*, vol. 57, no. 11, pp. 4355–4368, Nov. 2009.

[10] N. Dobigeon and N. Brun, "Spectral mixture analysis of EELS spectrum-images," *Ultramicroscopy*, vol. 120, pp. 25–34, Sept. 2012.

[11] N. Mevenkamp, B. Berkels, and M. Duchamp, "Denoising electron-energy loss data using non-local means filters," *Microsc. Microanal.*, vol. 23, no. S1, p. 106–107, 2017.

[12] O. Ledoit and M. Wolf, "A well-conditioned estimator for large-dimensional covariance matrices," *J. Multivariate Analysis*, vol. 88, no. 2, pp. 365–411, 2004.